Local Chemistry Engineering in Doped Photonic Glassfor Optical Pulse Generation

Jiejie Chen, Zhuo Shi, Shifeng Zhou, Zaijin Fang, Shichao Lv, Haohai Yu,* Jianhua Hao, Huaijin Zhang, Jiyang Wang, and Jianrong Qiu*

Abstract

The control of the optical response of multicomponent photonic glass through short- to medium-range chemistry design has led to the development of high-performance devices with efficient stimulated radiation, broadband optical amplification, and sensitive optical sensing. However, the success of optical modulation with an all-fiber configuration is limited by the difficulty in creating smart structural units that can dynamically switch light–matter interactions. Here, a local chemistry design strategy is reported that can help realize dynamic energy storage and its controllable release, based on the simultaneous management of the chemical state and ligand field of transition-metal dopant through glass crystallization. The theoretical analysis indicates that a four-level configuration, such as that of tetrahedral Cr^{4+}, can enable efficient photon–electron–photon conversion. Experimental data further reveal that this configuration can be stable in nanostructured glass. A nanostructured fiber with perfect core-clad configuration is successfully fabricated by the melt-in-tube approach. The optical modulation function in bulk glass with estimated σ_{gs} and σ_{es} values of $(1.39 \pm 0.03) \times 10^{-16}$ and $(1.20 \pm 0.02) \times 10^{-16}$ cm^2, respectively, is also demonstrated. Therefore, a principal pulse laser device with operation wavelength at 1.06 μm and pulse duration of 176 ns is fabricated for the first time.

1. Introduction

A central theme in fiber photonics is the design and fabrication of novel optical materials and components for the establishment of all-fiber photonic system.[1–4] Photonic glass has been recognized as the ideal candidate for reaching this target due to its excellent plasticity, extremely low loss, and unique tunable optical prop- erties. The past decades have witnessed substantial progress in the development and fabrication of active photonic glass[5,6] and various types of efficient gain matrix activated with rare-earth and transition- metal dopants (e.g., Nd^{3+},[7] Er^{3+},[8] Tm^{3+},[9] and Ni^{2+}[10,11]). However, it is still chal- lenging to construct smart glass that hasan optical-modulation function, and a few material candidates can realize pulse generation.[12,13] The existing toolbox for obtaining pulsed laser mainly relies on methods such as external modulation through electro- or acousto-optical process, and saturable absorption based on semiconductor mirror[14] or single crystal,[15] gold composite,[16] graphene,[17] and low-dimensional materials.[18–21] For example, Cr^{4+}-doped crystalline materials, such as Cr^{4+}:YAG[22] and Cr^{4+}:Mg_2SiO_4,[23] have been used as saturable absorbers for passive Q switching to generate nano- second or even picosecond laser pulses. Although widely implemented in research, t hese methods have limitations for possible all-fiber integration because it requires extra optical elements. Moreover, the related basic materials (e.g., semiconductor, gold, and graphene) also suffer from long-term optical and thermal instability.

Here, we report an effective approach to endow the photonic glass with pulse generation function by local chemistry engineering in doped multicomponent glass. This method involves careful fostering of the local chemistry around the dopant in the amorphous stage and promoting its orientation through controllable glass crystallization. Accordingly, the dynamic electronic transition process and population inversion can be rationally tuned, leading to the intriguing pulsed electromagnetic radiation with designable period. Results highlight that this inherent local structure-based strategy may provide new opportunity for developing an all-fiber photonic system by doping engineering in photonic glass.

2. Theoretical Analysis

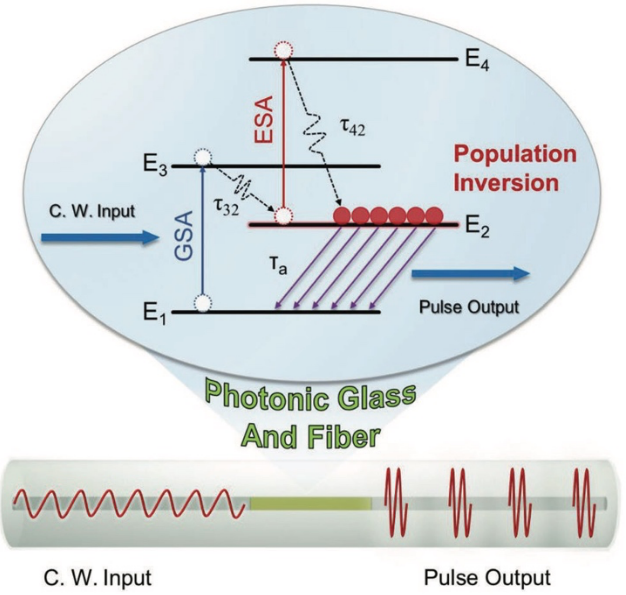

Figure 1. Schematic representation of the optical pulse generation in the photonic glass or fiber. The launched CW light interacts with the defined active region of the photonic glass or fiber, leading to a series of electronic transitions in the incorporated active species. The suitable electronic configuration and decay dynamics allow dynamic energy storage and its controllable release, resulting in the optical modulation with pulse generation. A typical four energy-level diagram is presented as a representative example.

The optical modulation for transformation of the continuous- wave (CW) into discrete photon packets involves dynamic energy storage and its controllable release. To achieve this goal in photonic glass, the most promising avenue is to rationally incorporate the dopants with appropriate energy levels, which can support electronic transitions in the interested waveband region. According to rate equation theory, the active dopant with four-level configuration is highly preferable for the realiza- tion of highly efficient photon–electron–photon conversion.[24] **Figure 1** shows that the dynamic process is associated with the saturation of $E1 \rightarrow E2$ electronic transitions, which is composed of the $E1 \rightarrow E3$ ground-state absorption (GSA) and $E3 \rightarrow E2$ non- radiative transitions. Moreover, excited-state absorption (ESA) from the metastable level $E2$ to a higher level $E4$ and $E4 \rightarrow E2$ relaxation transitions also occurs. Throughout the whole pro- cess, the corresponding population lifetimes of $E3 \rightarrow E2$ and $E4 \rightarrow E2$ (donated as $\tau 32$ and $\tau 42$; estimated to be approximately tens of picoseconds) are considerably shorter than that of $E2 \rightarrow E1$ (donated as $\tau \mathrm{a}$; estimated to be approximately a few microseconds). Under these conditions, the input CW with extremely high optical fluence may potentially accumulate the electrons in the

E_2 energy level and result in the population inversion of the system, finally leading to the pulse generation through the electron “avalanche” process.

The above processes can be quantitatively described using the following rate equations that provide valuable informa- tion about the energy-level populations and the photon density kinetics[25]

$$\frac{\mathrm{d}N_1}{\mathrm{d}t} = -N\sigma_{gs}\phi + \frac{N_2}{\tau_a} \tag{1}$$

$$\frac{\mathrm{d}N_2}{\mathrm{d}t} = N_1\,\sigma_{gs}\phi - N_2\sigma_{es}\phi + \frac{N_4}{\tau_{42}} - \frac{N_2}{\tau_a} \tag{2}$$

$$\frac{\mathrm{d}N_4}{\mathrm{d}t} = -N\sigma_{es}\phi - \frac{N_4}{\tau_{42}} \tag{3}$$

$$\frac{\mathrm{d}\phi}{\mathrm{d}t} = -\phi\left(N_1\sigma_{gs} + N_2\sigma_{es}\right) \tag{4}$$

where ϕ is the photo density of incident light, $N_0 = N_1 + N_2 + N_4$, (N_1, N_2, and N_4 are the populations in the ground state E_1, the first excited state E_2, and the second excited state E_4, respec- tively), σ_{gs} is the GSA cross section, σ_{es} is the ESA cross sec- tion ($\sigma_{gs} > \sigma_{es}$), and z is the coordinate along the longitudinal direction of the gain matrix. When the absorption saturation of E_2 is achieved, it is in the steady-state situation, where $N_1 \approx 0$, $N_0 \approx N_2$, and $\mathrm{d}N_1/\mathrm{d}t = \mathrm{d}N_2/\mathrm{d}t = 0$. Substituting Equations (1), (2), and (3) into (4), the following equation for instantaneous light intensity I and transmission T can be obtained

$$I = I_0 \exp\left(-\sigma_{gs}N_0L\right) \tag{5}$$

$$T = \frac{I_{\text{out}}}{I_{\text{in}}} = \frac{\phi_{\text{out}}}{\phi_{\text{in}}} = T_0\left(\frac{hv + \sigma_{es}\tau_a T I_{\text{in}}}{hv + \sigma_{es}\tau_a I_{\text{in}}}\right)^{1-\sigma_{gs}/\sigma_{es}} \tag{6}$$

where $I = hv$, hv is the photon energy, and L is the passage length of the gain matrix. I_0 is the incident light intensity, and T_0 is the initial transmission for the gain matrix. Equation (6)indicates that T increases rapidly as I_{in} increases until itremains constant, and the GSA is fully saturated. According to these relations, various physical parameters of the generated pulse such as pulse energy and width can be rationally engineered through the careful design of the local chemistry around the doped active centers.

Guided by theoretical analysis, chromium (Cr) was selected as the dopant in our research because of its unique electronic configuration. The primary advantage is that the energy-level configuration of tetra-coordinated Cr^{4+} ion is well consistent with the four energy-level model in Figure 1. Moreover, Cr^{4+} has a large GSA cross section and low saturation fluence, allowing highly efficient pulse generation. Furthermore, the electrons in outmost d orbitals of Cr^{4+} strongly interact with their ligands, to allow the tuning and optical modulation of the energy-level configuration in a wide waveband region.[26] The multicomponent glass system was studied as the potential matrix, owning to its rich microstructure and great tendency toward crystallization, which allows triggering of the local ordering for increasing the dopant orientation. The hybrid germanium silicate glass was finally selected because most of the topological units in this system are tetra-coordinated, which can potentially provide suit-able positions for Cr^{4+} for obtaining the desired four energy- level configuration.[27]

3. Results and Discussion

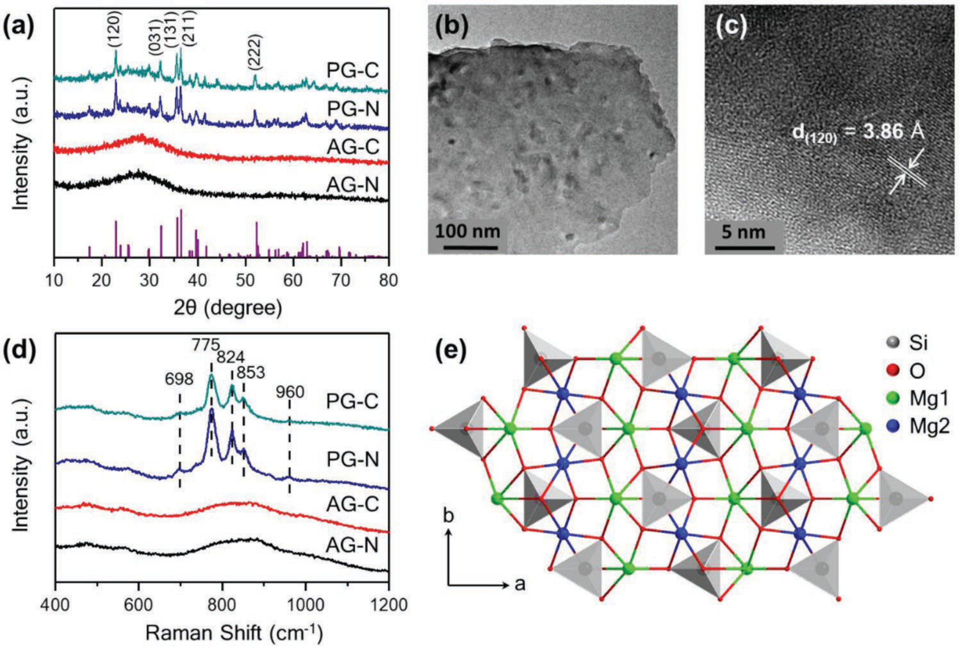

Figure 2. Structural features of the constructed photonic glass. a) XRD patterns of the AG-N, AG-C, PG-N, and PG-C samples. b) TEM and c) HRTEM images of the PG-N sample. d) Raman spectra of the AG-N, AG-C, PG-N, and PG-C samples. e) Polyhedral representation of the forsterite structure in a projection onto the *ab*-plane, showing the arrangements of the Mg1 and Mg2 octahedra.

Table 1. Nominal composition and heat-treatment temperature of the samples (in mol%).

Sample	SiO_2	GeO_2	Al_2O_3	Mg_2CO_3	K_2CO_3	KNO_3	TiO_2	Cr_2O_3	Temperature
AG-C	39.3	9.7	8.5	31.1	8.5	—	2.9	0.1	—
AG-N	39.3	9.7	8.5	31.1	—	17	2.9	0.1	—
PG-C	39.3	9.7	8.5	31.1	8.5	—	2.9	0.1	850 °C
PG-N	39.3	9.7	8.5	31.1	—	17	2.9	0.1	850 °C

To obtain the suitable composition of the photonic glass, a systematic study was conducted by referring the standard phase diagram of $SiO_2/GeO_2/MgO$. The final optimum composition was found to be $SiO_2/GeO_2/Al_2O_3/MgO/K_2O/TiO_2$ = 39.3/9.7/8.5/31.1/8.5/2.9 in mol%. Differential thermal analysis (DTA) was employed to characterize the glass crystallization process (Figure S1, Supporting Information). The estimated values for glass transition (T_g) and crystallization temperature (T_c) were 650 and 850 °C, respectively. Differential scanning calorimeter (DSC) was used to characterize the heat capacity (C_p) curves of the hyperquenched wool fibers (Figure S2, Supporting Information). The sub-T_g exothermic relaxation peak was between 527 and 707 °C, followed by an endothermic peak responsible for glass transition. The observed sub-T_g exothermic relaxation indicates the existence of structural heterogeneity.[28,29] The corresponding fictive temperature (T_f) was calculated to be ≈863 °C by using the energy-matching method.[30,31] Based on the thermal analysis, the glass crystallization was conducted at ≈850 °C to obtain the nanostructured glass. Moreover, two different types of K_2O precursor, K_2CO_3 and KNO_3, were compared for studying the effect of local reaction environment on the chemical state of the doping species. The constructed samples with various process conditions are summarized in **Table 1**. X-ray powder diffraction (XRD) was utilized to investigate the structural properties of various samples. In the XRD patterns (**Figure 2**a), the broad peaks in the as-made glass samples (AG-C and AG-N) indicate their amorphous nature. By contrast, the nanostructured samples (PG-C and PG-N) show similar sharp diffraction peaks, which can be ascribed to the precipitation of forsterite (Mg_2SiO_4; JCPDS File No. 34-0189) nanocrystals during crystallization. The mean particle size of the precipitated Mg_2SiO_4 crystals was determined using Scherrer's equation. Four diffraction peaks with the highest intensity at (211), (131), (120), and (031) were independently used for the calculation of crystalline size. The values were then averaged, and the final values are 25–28 nm for the PG-C and PG-N samples. A typical trans- mission electron microscope (TEM) image of the PG-N sample(Figure 2b) shows that nanocrystals are monodispersed in the glassy matrix. The high-resolution TEM (HRTEM) image ofa single particle (Figure 2c) indicates that the corresponding interplanar spacing is ≈3.86 Å, which matches well with the (120) planes of Mg_2SiO_4. The results are consistent with the XRD data. According to the Rayleigh–Gans model,[32] the com-posite with nanocrystals that are homogeneously dispersed in glassy matrix and have tiny crystallite size (<30 nm) is favorable for achieving excellent light transmission. These collaborative results confirm that the constructed nanostructured samples meet the qualifications well, thus demonstrating the great potential for photonic applications.

The critical physical parameter for realizing efficient optical modulation relies on the local chemistry for the effective activation of transition-metal dopant. Figure 2e shows that the for- sterite structure has an orthorhombic symmetry with a space group of P_{bnm} and four formula units in the unit cell. Its topo- logical feature is characterized by the isolated SiO_4 tetrahedra that are surrounded by MgO_6 octahedra, occupying sites of two different symmetries. Raman scattering spectroscopy was employed to study the topological structure of the samples. Figure 2d shows that no sharp Raman bands can be observedin the AG-N and AG-C samples, confirming their amorphous state. By contrast, several sharp peaks can be observed in the PG-N and PG-C samples. Previous studies indicate that Raman-active modes have no Mg1 motion (inversion sym metry) but can have Mg2 motion (mirror plane symmetry).[33] The strongest peak at 775 cm^{-1} can be ascribed to the symmetric stretching vibrations of Si–O–Si dimer linkages, as usu- ally observed in Si_2O_7 pyrosilicate structures. The peaks at 824,853, and 960 cm^{-1} are assigned to a mixed contribution of the symmetric (ν_1) and anti-symmetrical (ν_3) stretching modes of Si–O_{nb} in the SiO_4 tetrahedra (O_{nb} = nonbridge oxygen). The weak peak at 698 cm^{-1} is derived from the antisymmetrical stretching vibration of Si–O_b–Si (O_b = bridge oxygen).[33] These results demonstrate that the precipitated crystalline phase after glass crystallization can provide rich regular tetra-coordinated positions for the Cr^{4+} dopant. Furthermore, it is noteworthy thatreplacing the K_2CO_3 by using KNO_3 precursor may increase thequantity of the precipitated forsterite phases (Figure 2a,d), thus providing an effective avenue for the efficient activation of Cr^{4+} dopants.

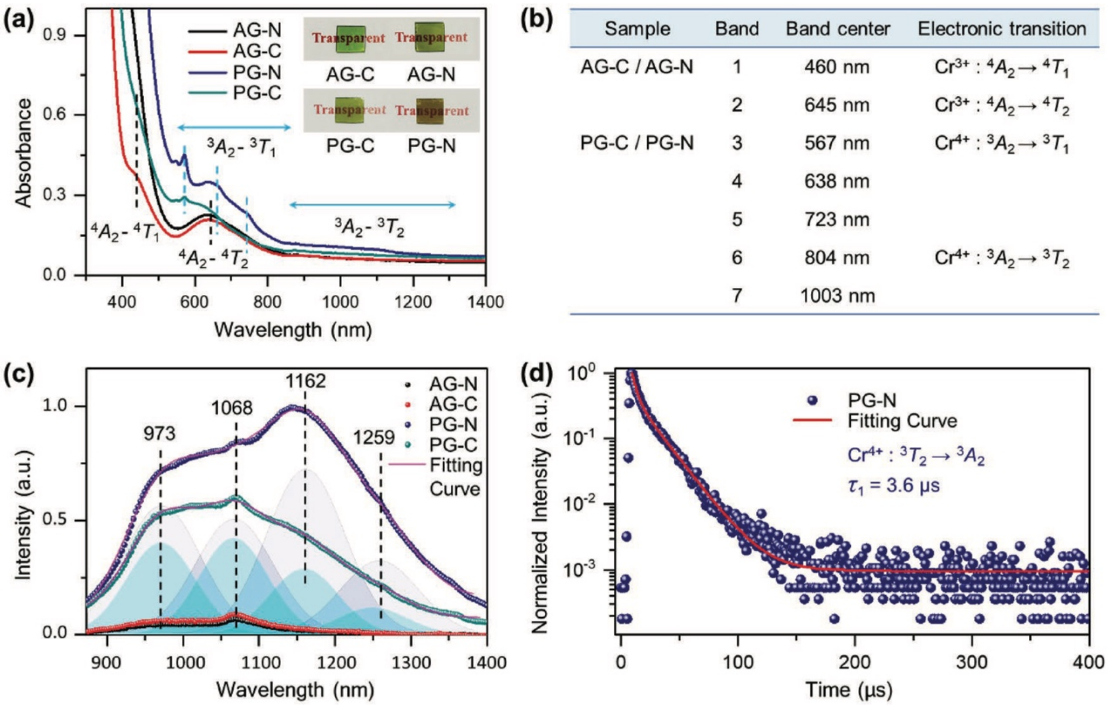

Sample	Band	Band center	Electronic transition
AG-C / AG-N	1	460 nm	Cr^{3+} : $^4A_2 \rightarrow {}^4T_1$
	2	645 nm	Cr^{3+} : $^4A_2 \rightarrow {}^4T_2$
PG-C / PG-N	3	567 nm	Cr^{4+} : $^3A_2 \rightarrow {}^3T_1$
	4	638 nm	
	5	723 nm	
	6	804 nm	Cr^{4+} : $^3A_2 \rightarrow {}^3T_2$
	7	1003 nm	

Figure 3. Spectral characteristics of the constructed photonic glass. a) Absorption spectra, and b) the corresponding electronic transitions of the AG-C, AG-N, PG-C, and PG-N samples. The insets of (a) show the photographs of the samples. c) NIR luminescence comparison of Cr ions in the glass and nanostructured samples under excitation with an 808 nm laser diode. Four Gaussian emission bands (blue peaks for PG-C and purple peaks forPG-N) are originated from the Cr^{3+}:$^4T_2 \rightarrow {}^4A_2$ (973 and 1068 nm) and Cr^{4+}:$^3T_2 \rightarrow {}^3A_2$ transitions (1162 and 1259 nm). d) Decay curve of the $^3T_2 \rightarrow {}^3A_2$ transition of Cr^{4+} in the PG-N sample at a wavelength of 1162 nm (excited at 680 nm). The decay curve was fitted with the double-exponential functions to calculate the rise and decay time by using the following equation: $y = y_0 + A_1\exp^{-(x-x_0)/\tau_1} + A_2\exp^{-(x-x_0)/\tau_2}$. In this study, between the two terms, only thedominant lifetime (τ_1) was used for comparison to investigate the temporal behavior.

To study the chemical state of the dopant and its local chemistry feature, steady optical absorption spectroscopy was employed to probe various characteristic electronic transitions. Results are presented in **Figure 3**a, and the corresponding classification is summarized in Figure 3b. The absorption bandscentered at 460 and 645 nm are ascribed to the spin-allowed butparity-forbidden $^4A_2 \rightarrow {}^4T_1$ and $^4A_2 \rightarrow {}^4T_2$ transitions of Cr^{3+} in the amorphous surroundings, respectively. Intense absorption shoulder is assigned to the parity allowed charge-transfer transitions of Cr^{6+}.[34] The multiple absorption bands at ≈500–800 and 850–1200 nm are attributed to the $^3A_2 \rightarrow {}^3T_1$ and $^3A_2 \rightarrow {}^3T_2$transitions of Cr^{4+} with energy-level splitting in a distorted tetrahedron, respectively.[35] These results provide two important clues: On one hand, nanocrystallization notably enhances the transition probability of the $^3A_2$

$\rightarrow {}^3T_1$ and ${}^3A_2 \rightarrow {}^3T_2$ transitions of Cr^{4+}, confirming the selective incorporation of Cr^{4+} into the regular positions because these transitions are greatly sup- pressed in distorted position.[36] Most probably, Cr^{4+} ions occupy tetrahedral Si-occupied sites in forsterite phases. On the other hand, in the nanostructured samples, the absorption intensity of Cr^{4+} in the PG-N sample is approximately two times higher than that in the PG-C sample. Results indicate that Cr^{3+} was successfully oxidized into Cr^{4+} under the oxidizing atmosphere produced by the decomposition of KNO_3 during melting. It can be confirmed by the absorption shoulder in the oxidizing-agent- containing samples (AG-N and PG-N) that obviously moves toward longer wavelength compared with those in the neutral- agent-containing samples (AG-C and PG-C). These changes can also be directly attributed to the appearance of the sample; the color of both samples changes dramatically after thermal crystallization (insets of Figure 3a).

The chemical state and local chemistry of the dopant can also be analyzed using the steady luminescence spectra. Figure 3c compares the luminescence feature of various samples under an excitation of an 808 nm laser diode. All samples exhibit broadband near-infrared (NIR) luminescence and importantly, nano crystallization substantially enhances the luminescence intensity (≈7 times). This phenomenon confirms the selective incorporation of the Cr dopant into the forsterite phases because the regular crystalline position with high crystal-field strength highly favors the increase in radiative transition. Moreover, a notable contrast in the spectral shape between PG-N and PG-C sample can be observed. To clarify the physical mechanism, spectral analysis was performed, and the luminescence band was decomposed into various Gaussian emission bands. The emission bands at 973 and 1068 nm can be ascribed to the ${}^4T_2 \rightarrow {}^4A_2$ transition of Cr^{3+}, and another two bands at 1162 and 1259 nm originated from the ${}^3T_2 \rightarrow {}^3A_2$ transition of Cr^{4+}.[35] Hence, the luminescence from Cr^{3+} and Cr^{4+} in sample PG-N are both stronger than that in sample PG-C. The enhanced luminescence is partially associated with the increased crystallinity, which has been evidenced in the structural analysis results (Figure 2a). More interestingly, the calculated Cr^{3+} and Cr^{4+} emission in the PG-N sample is ≈1.3 and ≈2.6 times stronger than that in the PG-C sample, respectively. The notable ratio difference originated from the change in the quantity of optically active ions, and the addition of KNO_3 oxidizing agent contribute greatly to the quantity enhancement of Cr^{4+} species. The decay process of the 1162 nm emission band at room temperature is examined and the fitted decay time of the ${}^3T_2$ excited state level is ≈3.6 μs (Figure 3d). The decay dynamics exactly correspond to the desired transition proposed in the four-level configuration (Figure 1), demonstrating the great potential of Cr-doped photonic glass for dynamic energy storage and controllable release.

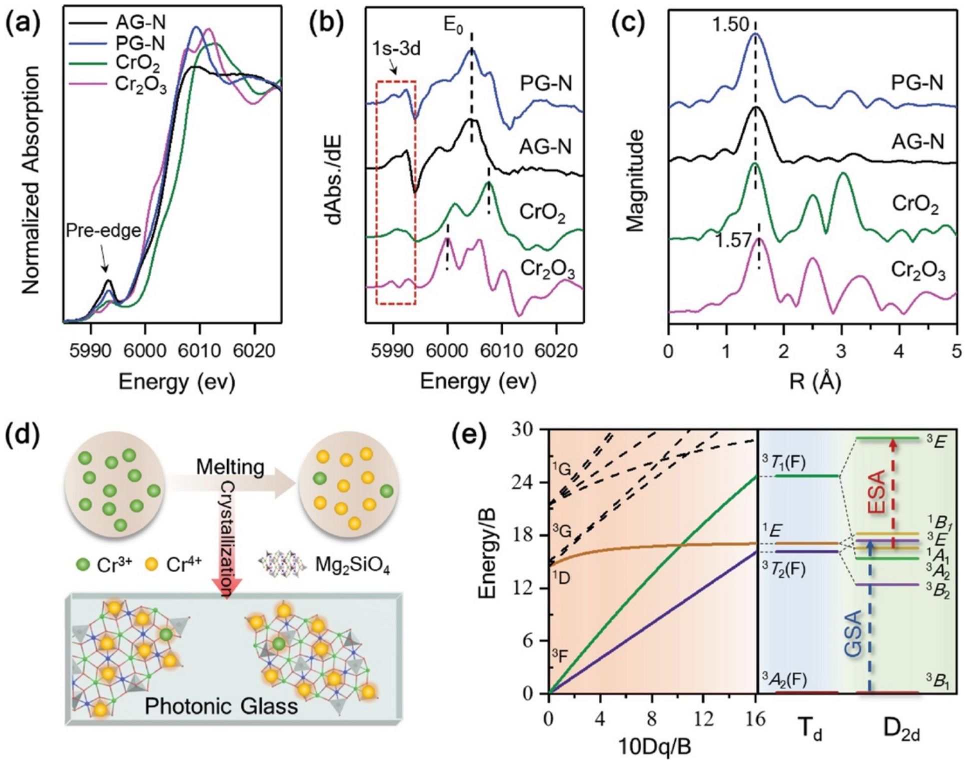

Figure 4. Local chemistry of the dopant in the constructed photonic glass. a) Cr K-edge XANES spectra. b) Derivative spectra of the XANES data.c) Fourier transform of the k^3-weighted EXAFS region of the AG-N and PG-N samples, compared with the standard samples of Cr_2O_3 and CrO_2. d) Schematic model indicating the phase evolution and dopant redistribution during glass crystallization. e) Schematic energy-level splitting processof the Cr^{4+} species in the T_d and D_{2d} symmetry based on the Tanabe–Sugano matrix.

Table 2. E_0 and E_p of chromium oxide compounds and Cr-doped AG-N and PG-N samples.

Energy[a)]	Cr_2O_3	CrO_2	AG-N	PG-N
E_0 [eV]	6000	6007.2	6004.5	6004.2
E_p [eV]	5990.4/5994.1	5990.9/5993.3	5990.7/5993.2	5990.7/5993.2

[a)] Uncertainties of E_0 and E_p are both ±0.5 eV.

X-ray absorption near edge structure (XANES) and extendedX-ray absorption fine structure (EXAFS) spectroscopy were employed to further validate the chemical state and local chem-istry change of the dopant.[37] **Figure 4**a shows the XANES spectra of the AG-N and PG-N samples and the two reference chromium oxide compounds. The spectra display several notable features. The two peaks at 6009 and 6019 eV in the PG-N sample are much sharper than that in the AG-N sample, indicating the improvement of the local environment symmetry of the Cr ions during crystallization. Although the chemical shift from Cr_2O_3 to CrO_2 is evident, it is difficult to precisely determine the edge energy due to the complex line shape with at least two inflection points in the Cr K-edge region.[38] Fortunately, the derivative spectra of the XANES data clearly show the trend of the absorption curve (Figure 4b). The corresponding main-edge energy (E_0) and pre-edge energy (E_p) of chromium oxide compounds and Cr-doped AG-N and PG-N samples were calculated and displayed in **Table 2**. The E_0 value indicates great oxidation-state dependence, which is frequently employed to determine the chemical-state change in transition-metal dopants such as Cr, Mn, Fe, and V.[39] As a typical example, the E_0 value of two reference chromium oxide compounds becomes large with the increase in the oxidation state of the chromium, which is ≈6000.0 eV for Cr^{3+} and ≈6007.2 eV for Cr^{4+}. Notably, in the Cr-doped AG-N and PG-N samples, the E_0 value is ≈6004 eV, which is between that of the standard samples of Cr_2O_3 and CrO_2. Results firmly suggest that Cr^{4+} and Cr^{3+} coexist in these two samples. The pre-edge region appearing in the Cr K-edge is attributed to a bound-state 1s to 3d transition. The pre-edge feature of the AG-N and PG-N samples is close to the CrO_2 reference, indicating the considerable presence of Cr^{4+}.[40] The radial structure function, yielded by the Fourier transform of the k^3-weighted EXAFS region reflects the local structure around the Cr species (Figure 4c).[41] Notably, the characteristic bands from Cr species in the PG-N sample are more prominent compared with that in the AG-N sample, indicating the high symmetry environment occupied by the Cr dopant after glass crystallization. The first band at ≈1.5 Å can be ascribed to the nearest Cr□O bonding, and the several following bands larger than 2 Å are associated with the Cr□Cr bonding. Notably, the nearest Cr□O bonding in the PG-N and AG-N samples is similar to that in CrO_2 (1.50 Å) but is smaller than that in Cr_2O_3 (1.57 Å). This fact implies that most Cr species in the PG-N and AG-N samples probably exist in the form of Cr^{4+}.[42] These results also collaboratively confirm that Cr^{4+} species, which are responsible for NIR absorption in the photonic glass, is likely occupied in the tetrahedral sites in the Mg_2SiO_4 phases. A schematic drawing was used to summarize the effects of glass melting and crystallization on the dopant evolution in the AG sample. Figure 4d shows that the addition of oxidizing agent may change the chemical equilibrium of $Cr^{3+} \rightarrow Cr^{4+}$ fractions and promote the formation of unusual Cr^{4+} centers. More importantly, glass crystallization leads to the precipitation of Mg_2SiO_4 crystalline phase, which helps to permanently fix the Cr^{4+} species in nanostructured photonic glass. Almost all Cr^{4+} species are segregated inside the nanocrystals, because the optical absorption of Cr^{4+} in the as-made glasses is vanished. According to the structural feature of Mg_2SiO_4, Cr^{4+} should be fourfold coordinated in the nanocrystals by substituting Si^{4+} in the distorted tetrahedral sites. The precipitation of ordered phase and the enhanced dopant orientation are crucial for achieving the desired electronic transitions as discussed in Figure 1. On one hand, the regular tetrahedral sites (T_d symmetry) around Cr^{4+} species split the ^3F ground-state level of the free-ion into three components: $^3F \rightarrow {}^3A_2 + {}^3T_2 + {}^3T_1$, and the distorted tetrahedron (D_{2d} symmetry) undergoes further orbital splitting.[24] Figure 4e shows that the energy-level diagram of Cr^{4+} in the nanostructured photonic glass is in good agreement with the desired four energy-level configuration. By using the equations given by solving the Tanabe–Sugano matrix,[43] the calculated values of crystal-field strength (D_q), and Racah parameters (B) from the fitting results of absorption spectra data in Figure S3 (Supporting Information), were $D_q = 1109\ \text{cm}^{-1}$ and $B = 675\ \text{cm}^{-1}$. On the other hand, the regular position in nanostructured glass with high crystal field strength may also change the electron relaxation process. According to the Mott and Gurney model, τ_n can be described by a single Arrhenius factor related to the occupation probability of the electrons in the vibrational excited state, given by $\tau_n = A\exp(-\Delta E/kT)$, where τ_n is the nonradiative decay time, A is a constant, k is the Boltzmann constant, ΔE is the activation energy, and T is the temperature.[44] Thus, nonradiative transitions need to over-come the potential barrier (i.e., ΔE). In this simple model, one would expect that the difficulty of the nonradiative decay process increases due to the high potential barrier generated by the high crystal field strength, resulting in high probability of room-temperature electronic transition process. Consequently, the rational control of the electronic transitions process through ligand-field engineering facilitates the dynamic energy storage and its controllable release.

Figure 5. Photonic glass fiber. a) Photographs of the cladding silica tube (diameter: ∅25 mm), the starting bulk glass (size ≈ 20 × 20 × 75 mm^3), andthe polished core glass rod (size: ∅3 mm × 40 mm). b) Photograph of the fabricated nanostructured fibers. c,d) Optical and SEM image of the nano-structured fiber cross section. e–h) EPMA images of the elemental distribution of Si, Mg, Al, and K in the nanostructured fiber cross section. Relative concentration is represented by the color bar.

We further tried to fabricate nanostructured photonic glass fiber. The constructed precursor glass belongs to a multicomponent glass system, which shows great tendency for phase separation or crystallization. To overcome this limitation, a novel melt-in-tube approach was employed. First, a large bulk glass with excellent optical quality was prepared using a quite slow annealing rate which of ≈0.1 °C min^{-1} from 615 to 25 °C. The bulk sample was reshaped into rod shape with an appropriate size and then inserted into the silica tube (**Figure 5**a). Second, fiber-drawing was performed under the extremely high temperature (≈1900 °C) to obtain a homogeneous glassy core, and fast drawing speed was used to avoid undesired phase separation. Third, the fabricated Cr-doped precursor glass fibers were thermally activated by annealing at 900 °C for 10 h and the obtained nanostructured photonic glass fibers are shown in Figure 5b. The thermal activation time is longer than that used for the bulk glass sample because the heat transfer efficiency is partly suppressed by the covered thick SiO_2 cladding. In the

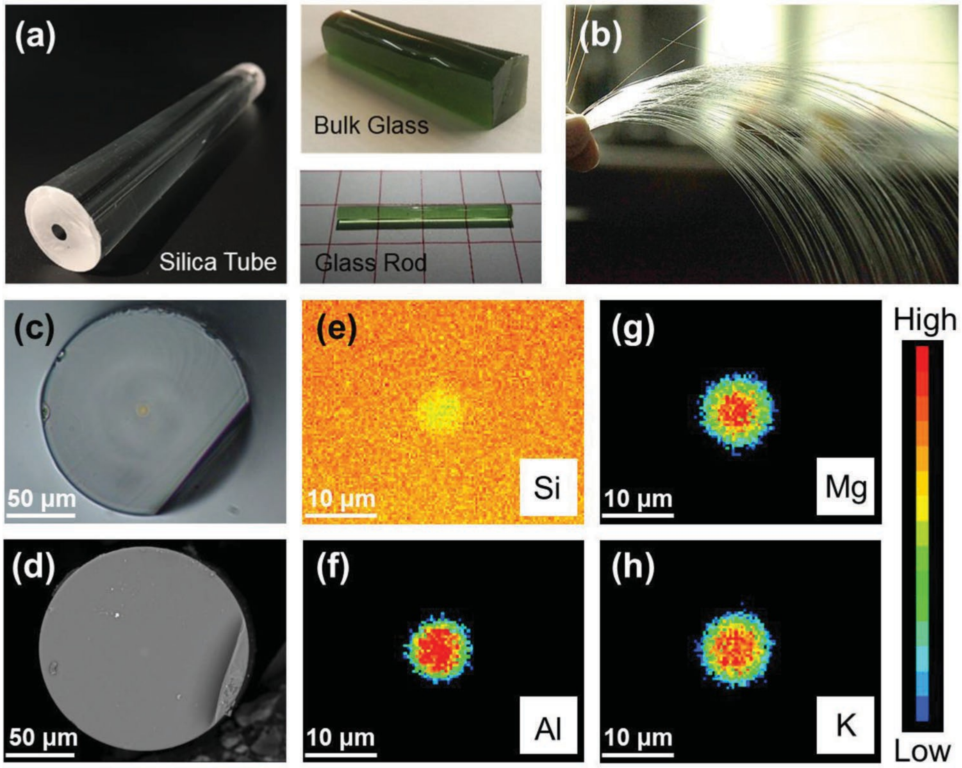

optical microscopy image of the nanostructured fiber cross section, the core regions are in yellow color, and the boundary between core and clad is clear (Figure 5c). The diameter of the fiber core and clad is ≈10 and 150 µm, respectively. Electron probe microanalysis (EPMA) measurement was performed on the cross section of the nanostructured fiber to determine the elemental distribution in the fiber core and clad (Figure 5d–h). Only the elements of Al, Mg, and K are enriched in the core region. These results indicate that negligible mutual diffusion occurs between the fiber core and clad during fiber-drawing and a nanostructured fiber with prefect core-clad configuration can be obtained.

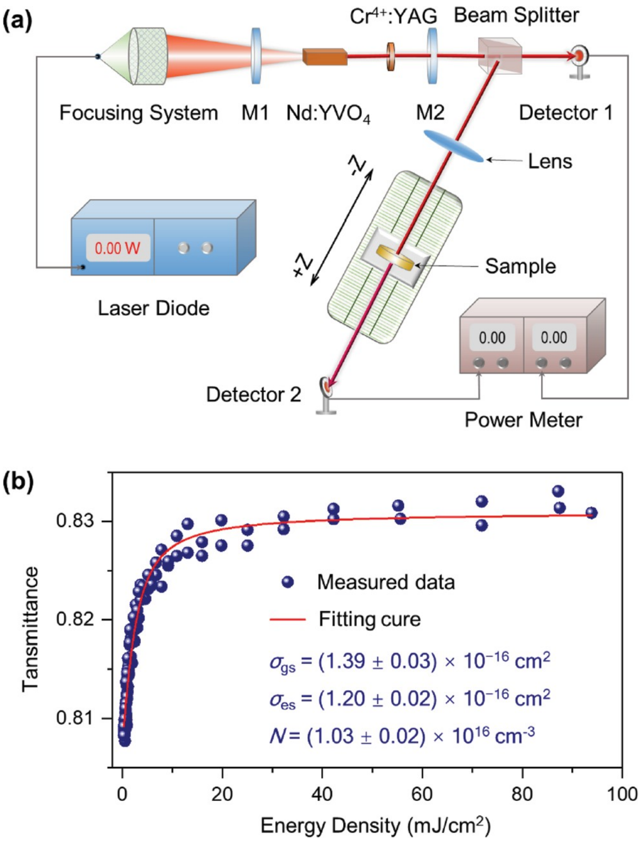

Figure 6. Nonlinear optical properties of the bulk photonic glass. a) Schematic diagram of Z-scan experiment setup. b) Dependence of the trans-mittance on the input energy density for the PG-N sample.

Based on the spectral properties of the photonic glass, nonlinear and saturable absorption would appear under the irradiation of high-intensity light due to the Pauli blocking of the electrons, which confers optical modulation properties to the photonic glass. The Z-scan optical setup was employed for the measurement of the nonlinear absorption of bulk glass. **Figure 6**a shows that the pump source was generated by a Q-switched Nd^{3+}:YVO_4 crystal laser with a pulse duration of 24 ns, repetition rate of

41.5 kHz, and wavelength of 1064 nm. The incident pulse energy can be tuned using an attenuator. Through a beam splitter, the laser beam was divided equally into two parts. One was measured with detector 1 for reference and the other was focused with a focus lens ($f = 50$ mm) and incidence vertical to the sample. The sample was placed on a displacement stage controlled by a step motor, which can movealong the *Z*-axis. Detector 2 was used to measure the beam powerafter the sample. Both the signal and reference branches were recorded using a two-channel power meter. In the Z-scan measurement, the beam radius ($\omega[z]$) depends on the sample position (z), which determines the incident energy intensity. For a typical Gauss beam,[45] it can be calculated by the following equation:

$\omega(z) = \omega_0(1 + z^2/z^{2})^{1/2}$, where ω is the focal radius, $z = k\omega_0^2/2$ is the Rayleigh length of the beam, $k = 2\Pi/\lambda$ is the wave vector, and λ is the laser wavelength. The values of ω_0 and z_0 in this experiment were 35 μm and 3.62 mm, respectively. The boundary conditions of the measurement are summarized as follows: Thesample length should be lower than z_0, and the distance betweenthe sample and detector 2 (d_2, estimated to be 250 mm) should beconsiderably higher than z_0.[46] Based on these boundary conditions, the photonic glass is strictly controlled to be 1.5 mm thick and carefully polished to achieve extremely high optical quality (surface roughness Ra < 10 nm). According to the *Z*-scan measurement, the nonlinear optical response process was obtained, which can be represented by the energy intensity-dependent transmittance (Figure 6b). From the figure, the transmission of the sample increases with the intensity of incident energy, and asaturation phenomenon was observed when the energy intensity reached the threshold (≈20 mJ cm^{-2}). The nonlinear absorption of the sample can be fitted using the Shimony model.[47] The transmission T is approximated as follows

$$T = \frac{E_{\mathrm{out}}}{E_{\mathrm{in}}} \cong T_0 + \frac{T_{\mathrm{i}} - T_0}{1 - T_0}(T_{\max} - T_0) \tag{7}$$

$$T_{\mathrm{i}} = \frac{h\nu}{\sigma_{\mathrm{gs}} E_{\mathrm{f}}} \ln\left\{1 + T_0\left[\exp\left(\frac{\sigma_{\mathrm{gs}} E_{\mathrm{f}}}{h\nu}\right) - 1\right]\right\} \tag{8}$$

where E_{in} is the incident pulse energy, E_{out} is the outgoingpulse energy, T_{i} is the energy transmission without the excited- state absorption, E_{f} is the incident pulse energy fluence, and$h\nu = 1.868 \times 10^{-19}$ J is the photon energy. $T_0 = \exp(-N\sigma_{\mathrm{gs}}L)$ is the initial transmission limit, and $T_{\max} = \exp(-N\sigma_{\mathrm{es}}L)$ is the sat-urated transmission limit, where N is the concentration of the tetrahedrally coordinated Cr^{4+} ions and L is the sample thickness. The experimental data can be well fitted to the Shimony model (Figure 6b), and the calculated values of σ_{gs} and σ_{es} are $(1.39 \pm 0.03) \times 10^{-16}$ and $(1.20 \pm 0.02) \times 10^{-16}$ cm^2, respectively, demonstrating the occurrence of strong dynamic energy storage and controllable release. The energy density threshold for triggering the optical modulation function in our sample is more than 100 times lower than that of other doped amorphous matrix.[48,49] This finding can be associated with the unique electronic transition processes in nanostructured photonic glass.

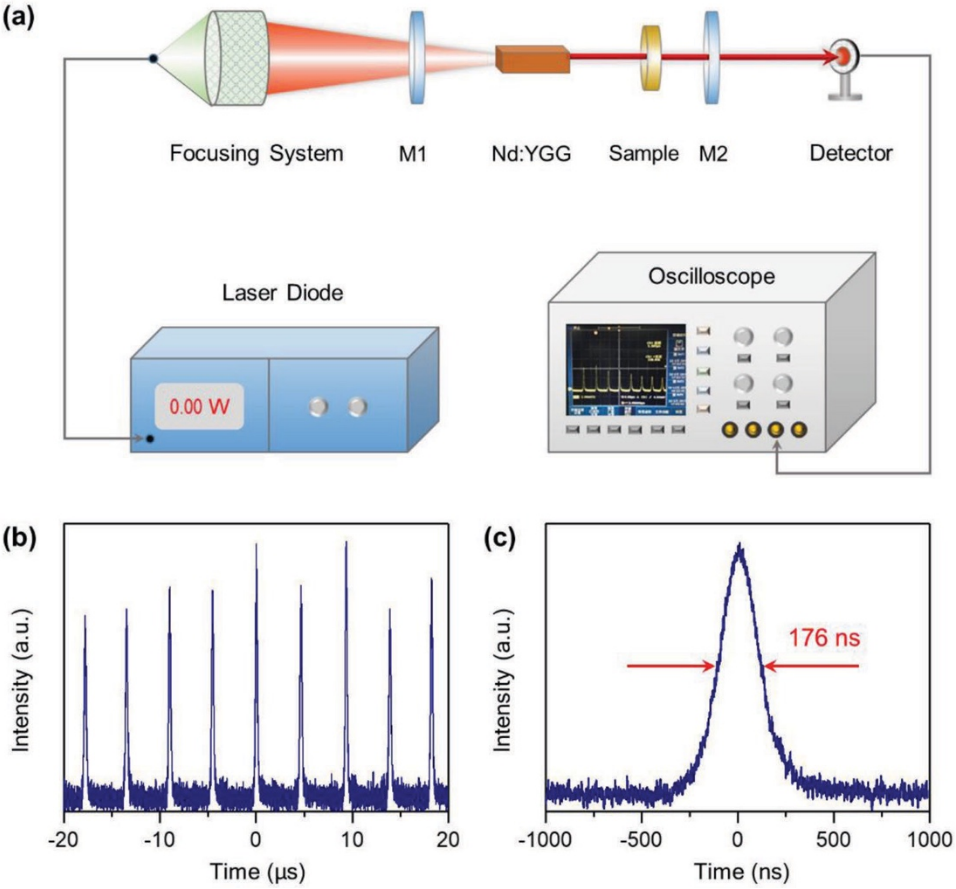

Figure 7. Pulse laser device based on the constructed bulk photonic glass. a) Schematic diagram of the principle pulse laser device. b,c) Pulse trainand profile of the PG-N sample with an absorbed pump power of 20 mW. The set of temporal pulse behavior of the original laser was recorded usinga TDS3012C digital phosphor oscilloscope (100 MHz bandwidth and 1.25 GS s^{-1} sample rate, Tektronix, Inc.).

The intriguing optical modulation properties realized in nanostructured photonic glass prompted us to design and fabricate novel principle pulse laser device. The schematic of the basic device configuration is shown in **Figure 7**a. The pump source consists of a fiber-coupled diode with a wavelength of 808 nm. M1 was a concave mirror with a curvature radius of 200 mm. It was anti-reflection-coated at 808 nm on the flat face, high-reflection-coated at 1.06 µm, and high-transmission-coated at 808 nm on the concave face. The output coupler M2 was a flat mirror with a transmission of 25% at 1.06 μm. The Nd:YGG crystal (size: 3 × 3 × 8 mm^3) was mounted on a water-cooled copper block, and the temperature of cooling water was maintained at 18 °C. The initial transmission of the PG-N sample at 1.06 μm was 80%. The nanostructured bulk sample was placed between the laser crystal and the OC. The cavity length was optimized to ≈30 mm. Encouragingly, the trace of laser pulse can be generated after modulation by the nanostructured photonic glass (Figure 7b). By contrast, no pulse can be observed without the modulation unit (Figure S4, Supporting Information). The produced pulse trace was stable, and the corresponding repetition rate was ≈250 kHz. A representative single pulse is highlighted in Figure 7c and the duration of the pulse was calculated to be ≈176 ns. Notably, this is the first trial, to the best of our knowledge, to endow the Cr-doped pho-tonic glass with a remarkable ability for dynamic energy storage and controllable release. Furthermore, based on the broad- band and flat absorption feature of the sample (Figure 3a), the acquired laser pulse was just limited by the available light source and pulse generation, and a wider frequency range from 800 to 1200 nm can be expected. Importantly, this is a good complement for Co-doped photonic glass, allowing the wavelength of the pulse to completely cover frequency range of 800–1700 nm.[50] By stark contrast to the conventional optical modulation component which is incompatible with the fiber device, the newly developed nanostructured photonic glass and fiber can be easily connected to the active fiber by thermal fusion. This property indicates its promising application in all- fiber photonic system. The newly developed material provides notable advantages of high laser-damage threshold, long-term optical stability, and excellent flexibility. The optical modulation properties of the fiber will be studied in the future.

4.Conclusion

Collaborative theoretical and experimental studies performed on Cr species in the amorphous matrix demonstrate the unique connection between the local chemistry of the dopant and the macroscale optical response of photonic glass. By precisely controlling the chemical state and ligand field of the dopant, the constructed nanostructured photonic glass can be endowed with intriguing optical modulation ability for laser pulse generation, indicating the promising opportunity for the construction of next-generation all-fiber photonic systems. This strategy should be general and versatile to other transition metals (e.g., Ni^{2+}, Co^{2+}, and Fe^{2+}) because of the similar electronic configuration with their outmost *d* orbital strongly interacting with the ligands. Our findings also serve as a valuable reference for the functionalization of other disordered systems with various properties such as luminescence, magnetic and electrical characteristics where dopants play a crucial role.

5. Experimental Section

Material Synthesis: Transparent precursor glasses were fabricated by the conventional melting-quenching method. The basic compositions of the material system were optimized to be $39.3SiO_2$-$9.7GeO_2$-$8.5Al_2O_3$- $31.1MgO$-$8.5K_2O$-$2.9TiO_2$ (in mol%) by referring to the standard phase diagram of $SiO_2/GeO_2/MgO$. High-purity (99.99%) Cr_2O_3 (0.1 mol%) was used as the raw doping agent. Potassium carbonate (K_2CO_3, 8.5 mol%) was used as neutral agent in the AG-C and PG-C samples. Potassium nitrate (KNO_3, 17 mol%) was used as oxidizing agent in the AG-N and PG-N sample. The oxidizing atmosphere can be obtained during the melting when KNO_3 was decomposed into K_2O, O_2, and NO gas. Following the typical synthesis, raw materials (20 g) were mixed thoroughly and melted in alumina crucibles at 1500 □C for 30 min under air atmosphere. The homogenized melt was cast into a slab on a preheated brass plate to form the precursor glass. Before optical characterizations, samples were cut into pieces of about 10 x 10 x 1.5 mm^3 and polished carefully.

Optical fibers were fabricated by the novel glass fiber-drawing technique named melt-in-tube. The glass compositions of the core fiber were kept at $39.3SiO_2$-$9.7GeO_2$-$8.5Al_2O_3$-$31.1MgO$-$8.5K_2O$-$2.9TiO_2$-$0.1Cr_2O_3$ (in mol%). A 200 g stoichiometric mixture of SiO_2, GeO_2, Al_2O_3, $MgCO_3{\cdot}4H_2O$, KNO_3, TiO_2, and Cr_2O_3 was mixed thoroughly in an agate mortar and melted in a Pt-Rh crucible at 1500 °C for 2 h. The glass melt was fabricated by pouring the melt into a preheated 20 x 20 x 75 mm^3 mold, and then annealed at 615°C for 3 h to release the inner stress. The bulk glass was burnished into a cylindrical rod with a diameter of 3.0 mm by using an abrasion wheel in lathe. The surface of the rod was polished and etched by acid to remove the contaminated surface layer. The rod was inserted into a high-purity (99.999%) silica tube with an inner hole diameter of 3.1 mm and an external diameter of 25.0 mm. The bottom of the tube was sealed to form a preform. Then, the preform was suspended in graphite furnace for drawing optical fibers. The temperature of the furnace was gradually increased to 1900 °C for melting the core glass and softening the clad glass tube. To effectively reduce the interdiffusion between the core and the clad, a fast drawing speed is required. In the fabrication method, the drawing speed was set at ≈15 m min^{-1}. The obtained precursor glass fibers were subsequently annealed at 900 °C for 10 h to obtain the desired nanostructured photonic glass fibers.

Material Characterization: DTA and DSC were employed in an STA449C Jupiter (STA449C, Netzsch, Germany) in argon atmosphere at a heating rate of 10 K $min^{□1}$. To determine the C_p curves of the hyperquenched wool fibers, both the baseline (blank) and the reference sample (sapphire) were measured. The fibers were subjected to two runs of upscans. The crystalline phases precipitated inside the glass were identified by XRD with Cu/K radiation (X'Pert Powder, PANalytical, Netherlands). Raman spectroscopy was employed using a Renishaw InVia spectrometer with a 532 nm laser source. The morphology and size distribution of the nanocrystals were analyzed by HRTEM (Tecnai G2 F20 s-twin, FEI, USA). Absorption spectra were recorded using a UV–vis–NIR spectrophotometer (Lambda-900, PerkinElmer, USA). The steady luminescence spectra under diode laser excitation (808 nm) were measured using a spectrometer (Omni k3007, Zolix, China) equipped with an InGaAs photodetector (R5108, Hamamatsu, Japan) and Stanford Research lock-in amplifier (SR830, SRS, Canada). The X-ray absorption spectra at the Cr K-edge were collected in the transmission mode by using a 1W1B beam line (XAFS station) at Beijing Synchrotron Radiation Facility. The ring energy was operated at 1.85 GeV and 205 mA. The X-rays were monochromatized using a Si (111) double-crystal spectrometer. The elemental distribution in the nanostructured fiber cross section was examined on an EPMA system (EPMA-1600, Shimadzu, Kyoto, Japan). All measurements were performed at room temperature.

Supporting Information

Supporting Information is available from the Wiley Online Library or from the author.

Acknowledgements

The authors gratefully acknowledge financial support from the National Key R&D Program of China (2018YFB1107200), the National Natural Science Foundation of China (Grant No. 11474102), the National Science Fund for Excellent Young Scholars of China (Grant No. 51622206), the Local Innovative and Research Teams Project of Guangdong Peal River Talents Program (Grant No. 2017BT01X137), the Tip-Top Scientific and Technological Innovative Youth Talents of Guangdong Special Support Program (Grant No. 2015TQ01C362), the Fundamental Research Funds for the Central University, and the Open Fund of State Key Laboratory of Information Photonics and Optical Communications (Beijing University of Posts and Telecommunications), P. R. China (IPOC2016B003).

Conflict of Interest

The authors declare no conflict of interest.

Keywords

local chemistry, photonic glass, pulse generation

Refence

[1] P. Russell, *Science* **2003**, *299*, 358.

[2] A. Sipahigil, R. E. Evans, D. D. Sukachev, M. J. Burek, J. Borregaard, M. K. Bhaskar, C. T. Nguyen, J. L. Pacheco, H. A. Atikian, C. Meuwly, R. M. Camacho, F. Jelezko, E. Bielejec, H. Park, M. Loncˇar, M. D. Lukin, *Science* **2016**, *354*, 847.

[3] W. Yan, A. Page, T. Nguyen-Dang, Y. Qu, F. Sordo, L. Wei, F. Sorin, *Adv. Mater.* **2018**, 1802348.

[4] S. F. Gao, Y. Y. Wang, W. Ding, D. L. Jiang, S. Gu, X. Zhang, P. Wang, *Nat. Commun.* **2018**, *9*, 2828.

[5] X. Liu, J. Zhou, S. Zhou, Y. Yue, J. Qiu, *Prog. Mater. Sci.* **2018**, *97*, 38.

[6] A. Jha, B. Richards, G. Jose, T. Teddy-Fernandez, P. Joshi, X. Jiang, J. Lousteau, *Prog. Mater. Sci.* **2012**, *57*, 1426.

[7] U. Skrzypczak, G. Seifert, S. Schweizer, *Adv. Opt. Mater.* **2015**, *3*,541.

[8] X. Xu, W. Zhang, D. Yang, W. Lu, J. Qiu, S. F. Yu, *Adv. Mater.* **2016**, *28*, 8045.

[9] Y. Liu, Y. Lu, X. Yang, X. Zheng, S. Wen, F. Wang, X. Vidal, J. Zhao, D. Liu, Z. Zhou, C. Ma, J. Zhou, J. A. Piper, P. Xi, D. Jin, *Nature* **2017**, *543*, 229.

[10] S. Zhou, N. Jiang, K. Miura, S. Tanabe, M. Shimizu, M. Sakakura, Y. Shimotsuma, M. Nishi, J. Qiu, K. Hirao, *J. Am. Chem. Soc.* **2010**, *132*, 17945.

[11] Y. Yu, Z. Fang, C. Ma, H. Inoue, G. Yang, S. Zheng, D. Chen, Z. Yang, A. Masuno, J. Orava, S. Zhou, J. Qiu, *NPG Asia Mater.* **2016**, *8*, e318.

[12] G. Karlsson, F. Laurell, J. Tellefsen, B. Denker, B. Galagan, V. Osiko, S. Sverchkov, *Appl. Phys. B* **2002**, *75*, 41.

[13] P. A. Loiko, O. S. Dymshits, V. V. Vitkin, N. A. Skoptsov, A. A. Kharitonov, A. A. Zhilin, I. P. Alekseeva, S. S. Zapalova, A. M. Malyarevich, I. V. Glazunov, K. V. Yumashev, *Laser Phys. Lett.* **2015**, *12*, 035803.

[14]D. Waldburger, S. M. Link, M. Mangold, C. G. E. Alfieri, E. Gini, M. Golling, B. W. Tilma, U. Keller, *Optica* **2016**, *3*, 844.

[15]H. Tanaka, R. Kariyama, K. Iijima, K. Hirosawa, F. Kannari, *Opt. Express* **2015**, *23*, 19382.

[16]T. Jiang, Y. Xu, Q. Tian, L. Liu, Z. Kang, R. Yang, G. Qin, W. Qin, *Appl. Phys. Lett.* **2012**, *101*, 151122.

[17]A. Martinez, Z. Sun, *Nat. Photonics* **2013**, *7*, 842.

[18]S. Wang, H. Yu, H. Zhang, A. Wang, M. Zhao, Y. Chen, L. Mei, J. Wang, *Adv. Mater.* **2014**, *26*, 3538.

[19]A. Autere, H. Jussila, Y. Dai, Y. Wang, H. Lipsanen, Z. Sun, *Adv. Mater.* **2018**, *30*, 1705963.

[20]Y. Zhang, D. Lu, H. Yu, H. Zhang, *Adv. Opt. Mater.* **2018**, *7*, 1800886.

[21]X. Liu, Q. Guo, J. Qiu, *Adv. Mater.* **2017**, *29*, 1605886.

[22]Y. Leng, H. Lu, L. Lin, Z. Xu, *Opt. Laser Technol.* **2001**, *33*, 403.

[23]M. I. Demchuk, V. P. Mikhailov, N. I. Zhavoronkov, N. V. Kuleshov, P. V. Prokoshin, K. V. Yumashev, M. G. Livshits, B. I. Minkov, *Opt. Lett.* **1992**, *17*, 929.

[24]Y. Kalisky, *Prog. Quantum Electron.* **2004**, *28*, 249.

[25]J. X. Wang, W. Z. Zhang, Q. R. Xing, Q. Y. Wang, *Opt. Laser Technol.* **1998**, *30*, 303.

[26]S. Zhou, C. Li, G. Yang, G. Bi, B. Xu, Z. Hong, K. Miura, K. Hirao, J. Qiu, *Adv. Funct. Mater.* **2013**, *23*, 5436.

[27]S. Zhou, Q. Guo, H. Inoue, Q. Ye, A. Masuno, B. Zheng, Y. Yu, J. Qiu, *Adv. Mater.* **2014**, *26*, 7966.

[28]Y. Zhang, G. Yang, Y. Z. Yue, *J. Am. Ceram. Soc.* **2013**, *96*, 3035.

[29]Y. Zhang, L. Hu, S. Liu, C. Zhu, Y. Z. Yue, *J. Non-Cryst. Solids* **2013**, *381*, 23.

[30]Y. Z. Yue, J. deC. Christiansen, S. L. Jensen, *Chem. Phys. Lett.* **2002**, *357*, 20.

[31]Y.-Z. Yue, *J. Non-Cryst. Solids* **2008**, *354*, 1112.

[32]G. H. Beall, L. R. Pinckney, *J. Am. Ceram. Soc.* **1999**, *82*, 5.

[33]D. A. McKeown, M. I. Bell, R. Caracas, *Am. Mineral.* **2010**, *95*, 980.

[34]J. Chen, Y. Yu, H. Luo, L. Lin, S. Zhou, *J. Am. Ceram. Soc.* **2018**, *101*, 159.

[35]V. A. Aseev, S. N. Zhukov, N. V. Kuleshov, S. V. Kuril'chik, A. V. Mudryi, N. V. Nikonorov, A. S. Rokhmin, A. S. Yasyukevich, *Opt. Spectrosc.* **2015**, *118*, 146.

[36]H. Krpplnn, *Am. Mineral.* **1992**, *77*, 62.

[37]J. J. Rehr, R. C. Albers, *Rev. Mod. Phys.* **2000**, *72*, 621.

[38]A. J. Berry, H. S. C. O'Neill, *Am. Mineral.* **2004**, *89*, 790.

[39]Y. G. Choi, K. H. Kim, Y. S. Han, J. Heo, *Chem. Phys. Lett.* **2000**, *329*, 370.

[40]O. Villain, G. Calas, L. Gaioisy, L. Cormier, J.-L. Hazemann, *J. Am. Ceram. Soc.* **2007**, *90*, 3578.

[41]G. N. Greaves, S. Sen, *Adv. Phys.* **2007**, *56*, 1.

[42]M. L. Peterson, G. E. Brown, G. A. Parks, C. L. Stein, *Geochim. Cosmochim. Acta* **1997**, *61*, 3399.

[43]Y. Tanabe, S. Sugano, *J. Phys. Soc. Jpn.* **1956**, *11*, 864.

[44]S. Zhou, G. Feng, B. Wu, N. Jiang, S. Xu, J. Qiu, *J. Phys. Chem. C* **2007**, *111*, 7335.

[45]M. Sheik-Bahae, A. A. Said, T. H. Wei, D. J. Hagan, E. W. Van Stryland, *IEEE J. Quantum Electron.* **1990**, *26*, 760.

[46]S. Wang, Y. Zhang, K. Wu, R. Zhang, H. Yu, H. Zhang, G. Zhang,Q. Xiong, *Opt. Lett.* **2015**, *40*, 2421.

[47]R. Feldman, Y. Shimony, Z. Burshtein, *Opt. Mater.* **2003**, *24*, 393.

[48]P. T. Guerreiro, S. Ten, N. F. Borrelli, J. Butty, G. E. Jabbour, N. Peyghambarian, *Appl. Phys. Lett.* **1997**, *71*, 1595.

[49]E. Wu, H. Chen, Z. Sun, H. Zeng, *Opt. Lett.* **2003**, *28*, 1692.

[50]V. Vitkin, P. Loiko, O. Dymshits, A. Zhilin, I. Alekseeva, D. Samitova, A. Polishchuk, A. Malyarevich, X. Mateos, K. Yumashev, *Appl. Opt.* **2017**, *56*, 2142.